# Instituto de Física
# Universidade de São Paulo

## The heavy-ion nuclear potential: determination of a systematic behavior at the region of surface interaction distances

**Silva, C.P.[a]; Alvarez, M.A.G.[a]; Chamon, L.C.[a]; Pereira, D.[a]; Rao, M.N.[a]; Rossi Jr., E.S.[a]; Gasques, L.R.[a] Santo, M.A.E.[b]; Anjos, R.M.[b]; Reis, Lubian, J.[b,e]; Gomes, P.R.S.[b]; Muri, C.[b]; Carlson, B.V.[c]; Kailas, S.[d]; Chatterjee, A.[d]; Singh, P.[d]; Shrivastava, A.[d]; Mahata, K.[d] and Santra, S.[d]**

[a] *Departamento de Física Nuclear, Instituto de Física, Universidade de São Paulo, São Paulo, Brasil*

[b] *Instituto de Física, Universidade Federal Fluminense, Niterói, Rio de Janeiro, Brasil*

[c] *Departamento de Física, Instituto Tecnológico de Aeronáutica, Centro Técnico Aeroespacial, São José dos Campos, São Paulo, Brasil*

[d] *Nuclear Physics Division, Bhabha Atomic Research Centre, Bombay, India*

[e] *Permanent addredd: CEADEN, P.O. 6122, Havana, Cuba*

Publicação IF - 1406/2000

UNIVERSIDADE DE SÃO PAULO
Instituto de Física
Cidade Universitária
Caixa Postal 66.318
05315-970 - São Paulo - Brasil

# The heavy-ion nuclear potential: determination of a systematic behavior at the region of surface interaction distances.

C. P. Silva[a], M. A. G. Alvarez[a], L. C. Chamon[a], D. Pereira[a], M. N. Rao[a], E. S. Rossi Jr.[a], L. R. Gasques[a], M. A. E. Santo[b], R. M. Anjos[b], J. Lubian[b,e], P. R. S. Gomes[b], C. Muri[b], B. V. Carlson[c], S. Kailas[d], A. Chatterjee[d], P. Singh[d], A. Shrivastava[d], K. Mahata[d] and S. Santra[d].

[a] *Laboratório Pelletron, Instituto de Física da Universidade de São Paulo, Caixa Postal 66318, 05315-970, São Paulo, SP, Brazil.*

[b] *Instituto de Física, Universidade Federal Fluminense, Av. Litoranea, Niterói, RJ, 24210-340, Brazil.*

[c] *Depto. de Física, Instituto Tecnológico de Aeronáutica, Centro Técnico Aeroespacial, São José dos Campos, SP, Brazil.*

[d] *Nuclear Physics Division, Bhabha Atomic Research Centre, Bombay 400 085 India.*

[e] *permanent address: CEADEN, P.O. 6122, Havana, Cuba.*

April 12, 2000

**Abstract**

Precise elastic scattering differential cross sections have been measured for the $^{16}O$ + $^{120}Sn$,$^{138}Ba$,$^{208}Pb$ systems at sub-barrier energies. The corresponding "experimental" nuclear potentials have been determined at interaction distances larger than the Coulomb barrier radii. These experimental potentials have been compared with our earlier results for other systems, and with theoretical calculations based on the double-folding and liquid-drop models. We have shown that the nuclear potentials have a systematic behavior at the surface region. The present results for the $^{16}O$ + $^{208}Pb$ system are used to extend earlier studies of the dispersion relation to sub-barrier energies.

NUCLEAR REACTIONS: $^{120}Sn(^{16}O, ^{16}O)^{120}Sn$, $^{138}Ba(^{16}O, ^{16}O)$ $^{138}Ba$, $^{208}Pb(^{16}O, ^{16}O)^{208}Pb$, measured elastic scattering cross sections. Deduced optical potentials. Double-Folding calculations with microscopic densities.

# I. Introduction

In this work, we present elastic scattering differential cross sections for the $^{16}O$ + $^{120}Sn$,$^{138}Ba$,$^{208}Pb$ systems at sub-barrier energies. The main purpose of the experiments was to determine the corresponding nuclear potentials. The method was applied earlier successfully to the $^{16}O$ + $^{58,60,62,64}Ni$, $^{88}Sr$, $^{90,92}Zr$, $^{92}Mo$ systems [1, 2, 3]. As discussed in these previous works, the imaginary part of the optical potential is negligible at sub-barrier energies due to the small number of reaction channels with relevant cross sections. Thus, the elastic scattering data analysis, at this energy range, determines the real part of the optical potential (nuclear potential). The slopes and strengths of the experimental (i.e. extracted from data analyses) nuclear potentials have been determined within 5% to 10% uncertainty in the surface region, $R \geq$ barrier radius $\simeq 1.4 \times (A_1^{1/3} + A_2^{1/3})$ $fm$.

The optical potential is the result of the addition of the bare and polarization potentials. The bare potential represents the ground state expectation value of the interaction operator, which contains as basic input the average effective nucleon-nucleon force. The polarization potential contains the contributions arising from nonelastic couplings. Due to the very small reaction cross sections, the absorptive imaginary part of the polarization potential is negligible at sub-barrier energies. We have estimated the contribution of the polarization potential to the real part of the optical potential to be small at the energy region at which our elastic scattering data were taken. Thus, the data extracted experimental potentials are representative of the corresponding bare potentials, and have been compared with those derived from double-folding and liquid-drop (proximity potential) theoretical models.

With the present work, we have completed a set of results (this work and Refs. [1, 2, 3]) to demonstrate a systematic behavior of the nuclear potential for systems involving the $^{16}O$ as projectile. All the target nuclei are magic or semi-magic, with mass number ranging from $A = 58$ to $A = 208$. The systematization indicates a universal exponential shape for the experimental potentials, as predicted by the liquid-drop model, but with a diffuseness value smaller than that from the proximity potential [4]. A similar result was found by Christensen and Winther (hereafter CW) [5] in another systematic study of potential strengths, which were extracted from elastic scattering data analyses at energies above the barrier. In that work, a diffuseness of 0.63 $fm$ was found for the heavy-ion nuclear potential, a value very close to that (0.62 $fm$) obtained from our sub-barrier data analyses. We have detected a small difference among the potential strengths at the sub-barrier region in comparison with those from the CW work. We have associated this difference to the following sources: i) variation with the energy of the polarization potential contribution to the optical potential, ii) variation of the bare potential with the energy, due to nonlocal effects, and iii) ambiguities in the extraction of potential strengths from the higher energy data analyses.

The polarization potential is expected to obey a dispersion relation [6] which

connects the real and imaginary parts of the optical potential. This relation has been observed for several systems [6], including $^{16}O$ + $^{208}Pb$ for which the dispersion relation had already been studied in a large energy range [7]. We have used our present results to extend this study to the sub-barrier region.

The paper is organized as follows: section 2 gives the experimental details and data analyses. In section 3, the experimental potentials are compared with those derived from double-folding and liquid-drop models. In section 4 is presented a comparison between potentials extracted from data analyses at the sub-barrier region with those from higher energies. The dispersion relation for the $^{16}O$ + $^{208}Pb$ system is analysed in section 5. Section 6 contains a brief summary and the main conclusions.

## II. Experimental Results and Data Analysis

The measurements for the $^{16}O$ + $^{120}Sn$,$^{138}Ba$ systems were made using the $^{16}O$ beam from the São Paulo 8UD Pelletron Accelerator, Brazil, and the data for the $^{16}O$ + $^{208}Pb$ system were taken at the 14UD BARC - TIFR Pelletron at Bombay, India. The detecting system has already been described in Ref. [1]. The thickness of the $^{120}Sn$, $^{138}Ba$ and $^{208}Pb$ targets were about 70 $\mu g/cm^2$. Figs. 1 to 3 exhibit the elastic scattering cross sections for the three systems in the energy ranges: $53 \leq E_{LAB} \leq 55\ MeV$ ($^{120}Sn$), $54 \leq E_{LAB} \leq 57\ MeV$ ($^{138}Ba$) and $74 \leq E_{LAB} \leq 78\ MeV$ ($^{208}Pb$). We have included a small contribution of detected transfer processes in the "elastic" cross sections for the $^{16}O$ + $^{208}Pb$ system.

In the optical model (hereafter OM) calculations, we have adopted a procedure similar to that described in the analysis of the sub-barrier elastic and inelastic scattering data for the $^{16}O$ + $^{58,60,62,64}Ni$, $^{88}Sr$, $^{90,92}Zr$, $^{92}Mo$ systems [1, 2, 3]. We have assumed a Woods-Saxon shape for the real part of the optical potential, with radius parameters equal to the Coulomb radii, which were obtained from electron scattering experiments [8]. We have also used an inner imaginary potential, which takes into account the rather small internal absorption from barrier penetration. The chosen parameters for this potential result in very small strengths at the surface region. This procedure must be adopted in the data analysis due to the small cross sections of peripherical reaction channels at sub-barrier energies. No sensitivity in the cross section predictions has been detected related to depth variations of this absorptive potential. The depth, $V_0$, and the diffuseness, $a$, of the (real) nuclear potential were searched for the best data fits. For each system and bombarding energy we have found a family of potentials, with different depth and diffuseness parameters, which give equivalent data fits, as illustrated in Fig. 4 for the $^{16}O$ + $^{208}Pb$ system at two different energies. These potentials cross at a particular radius, $R_S$, which is usually referred to as the strong absorption radius in the case of higher energy elastic scattering data analyses. At sub-barrier energies, this radius is related to the classical turning point, and is energy dependent. Due to the small absorption

involved in this case, we refer to $R_S$ as the sensitivity radius.

We have used the energy dependence of $R_S$ (see Fig. 5) to characterize the shape of the nuclear potentials at the surface region for the $^{16}O + {}^{120}Sn,{}^{138}Ba,{}^{208}Pb$ systems. For comparison purpose, we have included in Fig. 5 the earlier results [2, 3] that we had obtained for two lighter systems. As discussed in Ref. [1], the potential strength error bars were estimated considering the variation by unity of chi-square around the minimum value. The shape of the nuclear potential is quite close to an exponential, represented by solid lines in Fig. 5. Table 1 gives the diffuseness values obtained for the $^{16}O + {}^{120}Sn,{}^{138}Ba,{}^{208}Pb$ systems. We have included, in table 1, the results for the $^{16}O + {}^{58,60,62,64}Ni$, $^{88}Sr$, $^{90,92}Zr$, $^{92}Mo$ systems that we had obtained previously [1, 2, 3]. Within the uncertainties, the diffuseness parameters are compatible with the average value $\overline{a} = 0.62\ fm$. This diffuseness value is in good agreement with theoretical double-folding calculations, as will be discussed in the next section. Using the value $a = 0.62\ fm$, we are able to fit all the angular distributions (see Figs. 1 to 3) with an energy-independent nuclear potential for each system (which are represented by solid lines in Fig. 5). Table 1 also gives the radii ($R_{1\,MeV}$) at which the strengths of the energy-independent nuclear potentials equal 1 $MeV$, and the strengths at these same radii of the corresponding folding ($V_f$) and proximity ($V_{pr}$) potentials.

## III. Double-Folding and Proximity Calculations

In this section, we present theoretical calculations with the aim of evaluating the nuclear part of the ion-ion potential, by using the double-folding [9] and liquid-drop [4] models.

The double-folding potentials were calculated in a similar way as described in Refs. [1, 2, 3]. The ground-state nuclear density of the $^{16}O$ nucleus was derived from electron scattering experimental results [8], with the assumption that the neutron and proton densities have the same shape as the charge density. For the $^{208}Pb$ nucleus, we have used densities of Ref. [10] derived from Hartree-Fock calculations. For the neutron, $^{120}Sn$, and proton, $^{138}Ba$, superfluid (and semi-magic) nuclei, we have calculated nuclear densities using a self-consistent Dirac-Hartree-Bogoliubov model [11]. Fig. 6 presents the proton (dashed lines), neutron (dotted lines) and total (solid lines) densities for the $^{58}Ni,{}^{120}Sn,{}^{138}Ba$ and $^{208}Pb$ nuclei. For the heavier nuclei, the number of protons is significantly smaller than the number of neutrons, and the proton densities are somewhat more internal as compared to the corresponding neutron ones.

We have calculated the folding potential contributions of the proton and neutron target densities according to the following expressions:

$$V_p(R) = \int \rho_o(\vec{r_1})\ v_o\left(\vec{R} - \vec{r_1} + \vec{r_2}\right)\ \rho_p(\vec{r_2})\ d\vec{r_1}\ d\vec{r_2}, \qquad (1)$$

$$V_n(R) = \int \rho_o(\vec{r_1})\ v_o\left(\vec{R} - \vec{r_1} + \vec{r_2}\right)\ \rho_n(\vec{r_2})\ d\vec{r_1}\ d\vec{r_2}, \qquad (2)$$

$$V_f(R) = V_p(R) + V_n(R) = \int \rho_o(\vec{r_1})\, v_o\left(\vec{R} - \vec{r_1} + \vec{r_2}\right) \rho_t(\vec{r_2})\, d\vec{r_1}\, d\vec{r_2}, \qquad (3)$$

where $\rho_o$ is the total $^{16}O$ density; $\rho_p$, $\rho_n$ and $\rho_t$ are the proton, neutron and total target densities, respectively; $V_p$, $V_n$ and $V_f$ are the corresponding proton, neutron and total folding potentials. These folding potentials at the surface region are shown in Fig. 7. As expected, due to the neutron and proton density features, the heavier the target nucleus the greater is the neutron potential contribution in comparison to the corresponding proton one.

The predictions of the folding calculations for the potential strengths are smaller than the corresponding experimental values (see Table 1). We have previously [1, 2, 3] discussed this discrepancy for the $^{16}O$ + $^{58,60,62,64}Ni$, $^{88}Sr$, $^{90,92}Zr$, $^{92}Mo$ systems. These studies have indicated that the discrepancy is mainly connected to the $^{16}O$ nuclear density model adopted in the folding calculations [3].

Table 1 gives the "diffuseness parameters" obtained from the slopes of the folding potentials. The folding diffuseness values are similar for all systems and close to the average "experimental" value ($0.62\ fm$). This result indicates that the heavy-ion nuclear potentials have a "universal" shape in the surface region rather independent of the "size of the system". This behavior should be expected, considering that the features of the potential in the surface interaction region are dependent on the nuclear densities in the nucleus surface region, and that heavy-ions have very similar nuclear density diffuseness values, as detected for charge distributions from electron scattering experiments [8].

A theoretical interaction, which predicts a universal shape for the heavy-ion nuclear potentials, has been proposed [4] within the framework of the liquid-drop model. This interaction is based on the Proximity Theorem, which relates the force between two nuclei to the interaction between two flat surfaces made of semi-infinite nuclear matter. This theorem leads [4] to an expression for the potential which is a product of a simple geometrical factor and a universal function of the separation ($s = R - R_{C1} - R_{C2}$) between the surfaces of the nuclei

$$V(R) = 4\pi\gamma\bar{R}\alpha\ \Phi(s), \qquad (4)$$

with $\gamma = 0.9517(1 - 1.7826I^2)\ MeV/fm^2$, $I = \frac{N-Z}{A}$ and $\alpha \simeq 1\ fm$. The mean curvature of the system is obtained from

$$\bar{R} = \frac{R_{C1}R_{C2}}{R_{C1} + R_{C2}}. \qquad (5)$$

$R_{C1}$ and $R_{C2}$ are the central radii of both nuclei, which are related to the effective sharp radii by $R_{Ci} \simeq R_{eff,i}\ (1 - \alpha^2/R_{eff,i}^2)$. The formula indicated [4] for the effective sharp radius is

$$R_{eff,i} = 1.28A_i^{1/3} - 0.76 + 0.8A_i^{-1/3}. \qquad (6)$$

The universal function was calculated [4] using the nuclear Thomas-Fermi model with Seyler-Blanchard phenomenological nucleon-nucleon interaction [12, 13, 14]

$$\Phi(s \leq 1.2511\ \alpha) \simeq -\frac{1}{2}\left(\frac{s}{\alpha} - 2.54\right)^2 - 0.0852\left(\frac{s}{\alpha} - 2.54\right)^3, \qquad (7)$$

$$\Phi(s \geq 1.2511\,\alpha) \simeq -3.437 \exp\left(-\frac{s}{0.75\,\alpha}\right). \quad (8)$$

The proximity potential predicts an exponential shape at the surface region (Eq. 8), but with a diffuseness parameter (0.75 $fm$) greater than the value (0.62 $fm$) that we have obtained from data analyses. The radii $R_{1\,MeV}$ (see Table 1) at which the experimental potential strengths equal 1 $MeV$, correspond to separation distances about 3 $fm$. In this region, the strengths of the proximity potentials are about half of the corresponding experimental values (see Table 1). In the same region, similar differences among experimental results and theoretical predictions, concerning both diffuseness and potential strength values, had already been shown in the original paper in which the proximity potential was proposed (see Fig. 9 of Ref. [4]). We believe that such differences are due to the model adopted for the nuclear densities in the derivation of the proximity potential.

## IV. Systematization of the Nuclear Potential

The main features of the proximity potential are the universal shape and the dependence of the strengths with the mean curvature ($\bar{R}$) of the system. These features are also included in the empirical potential (Eq. 9) proposed by Christensen and Winther in the seventies [5]. In that work, the radii involved in the $s$ and $\bar{R}$ calculations were obtained from expression (10). The values $V_0 = 50\ MeV/fm$ and $a = 0.63\ fm$ were obtained from the fit of "experimental" potential strengths, extracted from elastic scattering data analyses for several systems at energies above the Coulomb barrier.

$$V(R) = -V_0 \bar{R} e^{-s/a} \quad (9)$$

$$R_{Ci} = 1.233 A_i^{1/3} - 0.978 A_i^{-1/3} \quad (10)$$

We have selected potential strength "data" from the CW systematization [5] for systems that involve the $^{16}$O nucleus. Fig. 8 (bottom) presents the $V/\bar{R}$ values as a function of the nucleus surface separation distance. The solid lines in the figure represent the CW empirical potential. Our sub-barrier strength "data" are also presented in Fig. 8 (top). The sub-barrier strength "data" are systematically greater than the CW empirical potential. The dashed lines in Fig. 8 represent a fit of the sub-barrier strength "data" to expression (9), which resulted the values $a = 0.61\ fm$ and $V_0 = 75.5\ MeV/fm$.

Fig. 8 (top) shows that the difference between sub-barrier strength "data" and the CW empirical potential is slightly dependent on the $s$ value. The average difference between the complete set of sub-barrier strength "data" and the CW empirical potential (solid lines in Fig. 8) is 18%. We point out that also the higher energy strength "data" for systems with $^{16}$O (Fig. 8 bottom) are, in average, slightly greater than the CW empirical potential. We estimate that the average difference among sub and above-barrier strength "data" is about 15%. Thus, the agreement between both analyses is good, and we have associated this

small difference to three sources: i) variation with the energy of the polarization potential contribution to the optical potential, ii) variation with the energy of the bare potential, due to nonlocal effects (this subject is discussed in the next section), and iii) ambiguities in the determination of the optical potential from elastic scattering data fits at energies above the barrier.

We have already extensively discussed [1, 2, 3] the contribution of the polarization potential to the nuclear potential strengths that we have obtained from sub-barrier data analysis for the $^{16}O$ + $^{58,60,62,64}Ni$, $^{88}Sr$, $^{90,92}Zr$, $^{92}Mo$ systems. Extensive and rather complete coupled channel (hereafter CC) calculations have indicated that the strengths of the polarization potential, at the energy range at which our sub-barrier data have been obtained, are about 17% of the bare potential strengths [3, 17], which corresponds to 14% of the optical (polarization + bare) potential. The contribution of the coupling for the $^{16}O$ $3^-$ state (which has a very large fonon amplitude) is about 50% of the full polarization potential (which corresponds to all coupled channels). Nevertheless, recent comparison [18] between the predicted fusion cross sections of this full CC analysis and precise fusion data indicates that such CC calculations overpredict the data at energies below the barrier (see Fig. 3 of Ref. [18]). Thus, we believe that the couplings are not so strong as considered in such CC calculations, and the polarization potential strength should be even less significant in comparison to the optical potential. Based on these studies, we estimate the contribution of the polarization potential to the experimental potentials extracted from sub-barrier data to be less than 10%. In this sense, we consider the experimental potentials at sub-barrier energies to be representative of the corresponding bare potentials.

In the sub-barrier elastic scattering data analysis, we have assumed the strengths of the imaginary part of the optical potential to be very small in the surface region. As we have already discussed, this procedure is consistent with the very small absorption in this energy region. At higher energies, it is very difficult to set the imaginary part of the optical potential based on physical grounds. Thus, the corresponding OM elastic scattering data analyses usually involve parametrized shapes (mostly the Woods-Saxon one) for the imaginary part of the potential, and this procedure results in ambiguities in the determination of the strengths of the real part of the optical potential. As an example, we have taken elastic scattering data for the $^{16}O$ + $^{208}Pb$ system [15, 16] in three energies, which are included in the CW potential strength systematization (open triangles in Fig. 8 - bottom). We have fitted the angular distributions (solid lines in Fig. 9) assuming the sub-barrier energy-independent nuclear potential for the real part of the optical potential. In these fits, only the diffuseness ($a_i$) and depth ($W_0$) of a Woods-Saxon shape (with $r_{i0} = 1.2\ fm$) imaginary potential were allowed to vary. Table 2 contains the resulting $a_i$ and $W_0$ values. Table 2 also presents a comparison among the potential strengths at the strong absorption radii of the present sub-barrier energy-independent potential ($V_{SB}$) with those ($V_{CW}$) obtained from the earlier OM data fits of Refs. [15, 16] (which were used in the CW systematization [5]). There are large differences between these sets of potential strengths, but the elastic scattering data fits obtained from both sets are equivalent. Thus, the strengths of the optical potential are

not well determined from data fits at energies above the barrier. We stress that the present sub-barrier data analysis determines the real part of the optical potential without ambiguity.

## V. The Dispersion Relation

Elastic scattering data analyses for some heavy-ion systems have resulted in a rapid and localized variation of the optical potential with the energy, known as "threshold anomaly" [6]. This variation has been observed in the vicinity of the Coulomb barrier, and has been associated to the contribution of the polarization to the optical potential [6]. The dispersion relation, Eq. (11) [6], describes the connection between the energy dependence of the real and imaginary parts of the polarization potential.

$$\Delta V(E) = \frac{P}{\pi} \int_{-\infty}^{\infty} \frac{W(E')}{E' - E}\, dE' \tag{11}$$

The $^{16}O + ^{208}Pb$ system is included among the systems for which the threshold anomaly was first observed [7]. The dispersion relation was verified for this system from the Coulomb barrier to higher energies. We have used the present results to extend these studies to the sub-barrier energy region. In an earlier work [3], we have made a similar study for the lighter systems. Fig. 10 presents the data extracted OM potential strengths from Ref. [7] (closed circles and open triangles) and the present sub-barrier results (open circles). The solid lines in the figure represent the trend suggested in Ref. [7], which is compatible with the dispersion relation.

In section 4, we have discussed the ambiguity in the determination of potential strengths from elastic scattering data analyses at energies above the Coulomb barrier. This sort of ambiguities is illustrated in Fig. 10. The open triangles in this figure correspond to earlier OM data analyses (from Ref. [7]) for the angular distributions presented in Fig. 9. The closed triangles in Fig. 10 represent the results of our OM analyses for the same angular distributions, in which the "sub-barrier" energy-independent nuclear potential was used for the real part of the optical potential. The differences between closed and open triangles provides an estimation about the "error bars" that the potential strengths may have. Thus, the trend adopted for the optical potential suggested based on the "data" behavior is itself also ambiguous. The ambiguity in the determination of potential strengths from OM elastic scattering data analysis at energies above the barrier could be reduced by using a realistic (based on fundamental physical grounds) imaginary part for the optical potential. A model for a realistic polarization potential should be consistent with the dispersion relation.

There is an additional energy dependence of the optical potential that arises from the nonlocal nature of the bare nuclear interaction [6]. This additional energy dependence has been neglected in most studies of the dispersion relation. Recently, a model for the energy dependence of the bare potential has been

proposed [19, 20]. For the $^{16}O + ^{208}Pb$ system and based on this model, we have calculated a variation of about 0.17 $MeV$ between the strengths (at $R = 12.4\ fm$) of the bare potential at $E_{LAB} = 60\ MeV$ and $E_{LAB} = 240\ MeV$. The difference between solid and dashed lines in Fig. 10 (top) represents the additional variation of the optical potential due to nonlocal effects in the bare potential.

## VI. Summary and Conclusions

In summary, we have performed optical model analyses of elastic scattering angular distributions for the $^{16}O + ^{120}Sn, ^{138}Ba, ^{208}Pb$ systems at sub-barrier energies. The sub-barrier data analyses determine the optical potential without the usual ambiguities found in elastic scattering data analyses at energies above the barrier. The present sub-barrier data are well reproduced with energy-independent nuclear potentials, which are real and have an exponential shape in the surface region. Similar results had been obtained by us earlier for the $^{16}O + ^{58,60,62,64}Ni$, $^{88}Sr$, $^{90,92}Zr$, $^{92}Mo$ systems. The diffuseness of all these experimental potentials are compatible, within the uncertainties, with the average value $\overline{a} = 0.62\ fm$. This result is in agreement with theoretical Double-Folding calculations, and with the Christensen and Winther's systematization of real potential strengths which were extracted from higher energy OM data analyses. Our sub-barrier results indicate a systematic behavior for the nuclear potential, which contains the main features predicted by the liquid-drop model. By combining exchange nonlocal effects and the liquid-drop model [21], it is possible to describe the heavy-ion nuclear potential in a much larger energy range than that considered in this work.

This work was partially supported by Financiadora de Estudos e Projetos (FINEP), Fundação de Amparo à Pesquisa do Estado de São Paulo (FAPESP), Fundação de Amparo à Pesquisa do Estado do Rio de Janeiro (FAPERJ), and Conselho Nacional de Desenvolvimento Científico e Tecnológico (CNPq).

# References

[1] L.C. Chamon, D. Pereira, E.S. Rossi Jr., C.P. Silva, R. Lichtenthaler Filho and L. C. Gomes, Nucl. Phys. **A582** (1995) 305.

[2] L.C. Chamon, D. Pereira, E.S. Rossi Jr., C.P. Silva, H. Dias, L. Losano and C. A. P. Ceneviva, Nucl. Phys. **A597** (1996) 253.

[3] M.A.G. Alvarez, L.C. Chamon, D. Pereira, E.S. Rossi Jr., C.P. Silva, L.R. Gasques, H. Dias and M.O. Roos, Nucl. Phys. **A656** (1999) 187.

[4] J. Blocki, J. Randrup, W. J. Swiatecki and C. F. Tsang, Ann. of Phys. **105** (1977) 427.

[5] P. R. Christensen and A. Winther, Phys. Lett. **B65** (1976) 19.

[6] G. R. Satchler, Phys. Rep. **199** (1991) 147.

[7] M. A. Nagarajan, C. C. Mahaux and G. R. Satchler, Phys. Rev. Lett. **54** (1985) 1136.

[8] C. M. De Jager, H. De Vries and C. De Vries, At. Data Nucl. Data Tables **14** (1974) 479.

[9] G. R. Satchler and W. G. Love, Phys. Rep. **55** (1979) 183.

[10] J. W. Negele, Phys. Rev. **C4** (1970) 1260.

[11] B. V. Carlson and D. Hirata, submitted to Phys. Rev. **C**.

[12] W. D. Myers and W. J. Swiatecki, Ann. Physics **55** (1969) 395.

[13] J. Randrup, Lawrence Berkeley Laboratory Report LBL-4302 (1975); Nucl. Phys. **A259** (1976) 253.

[14] R. G. Seyler and C. H. Blanchard, Phys. Rev. **124** (1961) 227; **131** (1963) 355.

[15] F. D. Becchetti, D. G. Kovar, B. G. Harvey, J. Mahoney, B. Mayer and F. G. Puhlhofer, Phys. Rev. **C6** (1972) 2215.

[16] J. B. Ball, C. B. Fulmer, E. E. Gross, M. L. Halbert, D. C. Hensley, C. A. Ludemann, M. J. Saltmarsh and G. R. Satchler, Nucl. Phys. **A252** (1975) 208.

[17] N. Keeley, J. S. Lilley and J. A. Christley, Nucl. Phys. **A603** (1996) 97.

[18] N. Keeley, J. S. Lilley, J. X. Wei, M. Dasgupta, D. J. Hinde, J. R. Leigh, J. C. Mein, C. R. Morton, H. Timmers and N. Rowley, Nucl. Phys. **A628** (1998) 1.

[19] M. A. C. Ribeiro, L. C. Chamon, D. Pereira, M. S. Hussein and D. Galetti, Phys. Rev. Lett. **78** (1997) 3270.

[20] L. C. Chamon, D. Pereira, M. S. Hussein, M. A. C. Ribeiro and D. Galetti, Phys. Rev. Lett. **79** (1997) 5218.

[21] L. C. Chamon et al., work in progress.

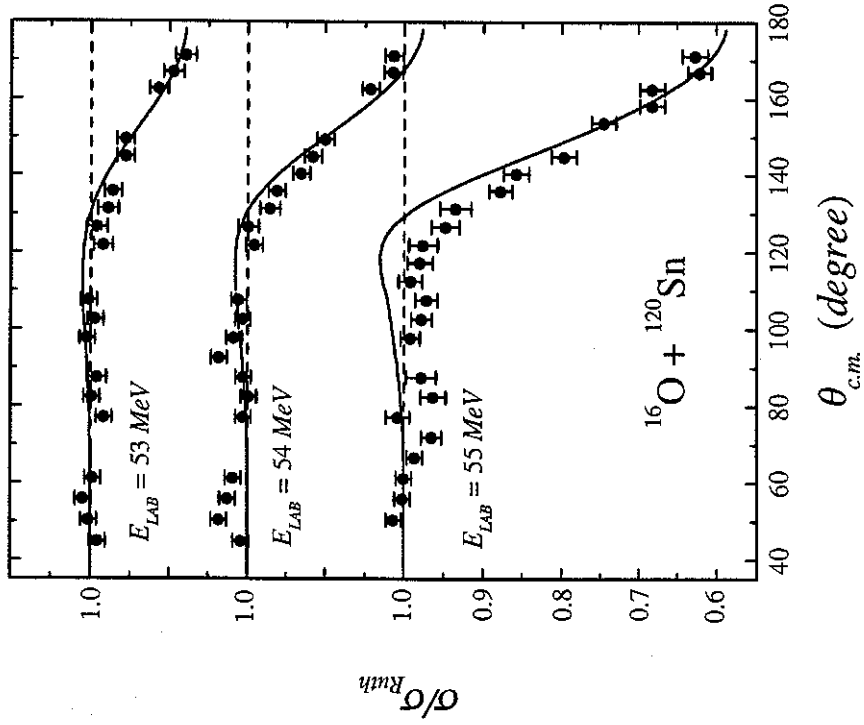


Figure 1: Elastic scattering angular distributions for the $^{16}O$ + $^{120}Sn$ system at the bombarding energies $E_{LAB}$ = 53, 54 and 55 $MeV$. The solid lines correspond to optical model calculations with an energy-independent nuclear potential, with diffuseness $a = 0.62\ fm$ (see details in the text).

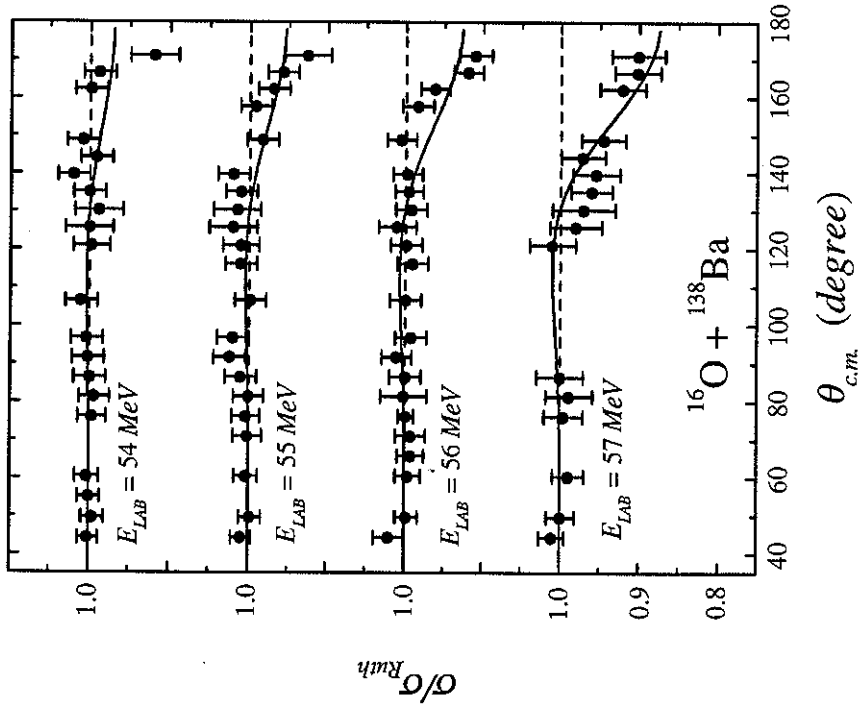


Figure 2: The same as in Fig. 1, for the $^{16}$O + $^{138}$Ba system at $E_{LAB}$ = 54, 55, 56 and 57 $MeV$.

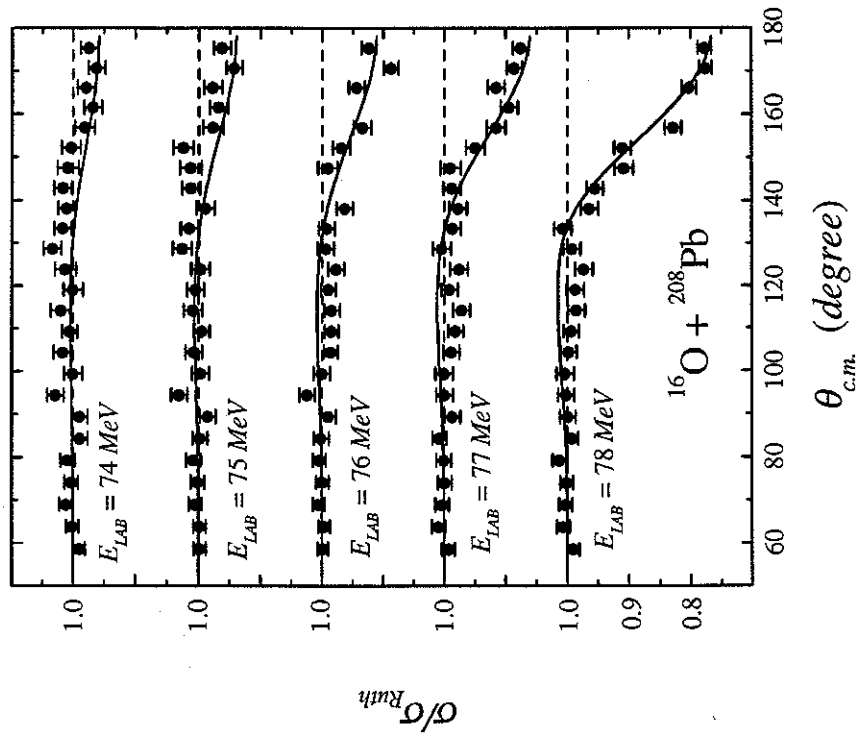


Figure 3: The same as in Fig. 1, for the $^{16}$O + $^{208}$Pb system at $E_{LAB}$ = 74, 75, 76, 77 and 78 $MeV$.

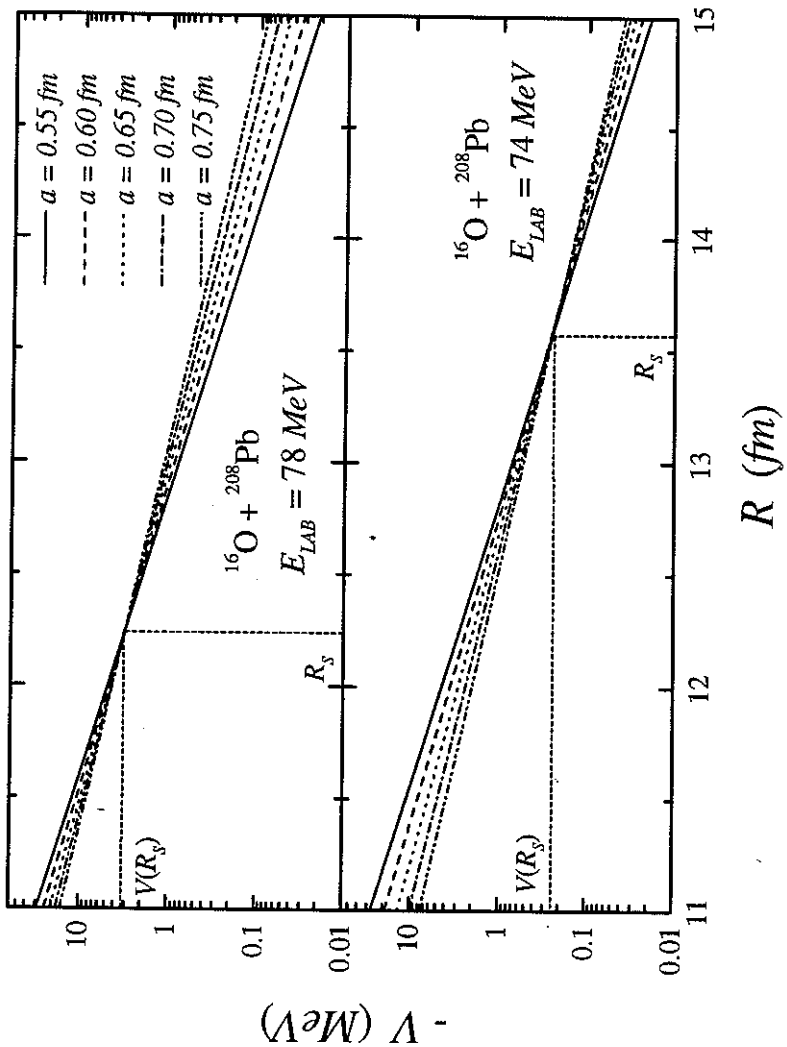


Figure 4: Determination of the nuclear potential at the sensitivity radius ($R_S$) for the $^{16}O + ^{208}Pb$ system, as obtained from OM analysis of the experimental data ($E_{LAB} = 74$ and $78\ MeV$). The lines represent potentials with different values of diffuseness and depth parameters, which give equivalent data fits.

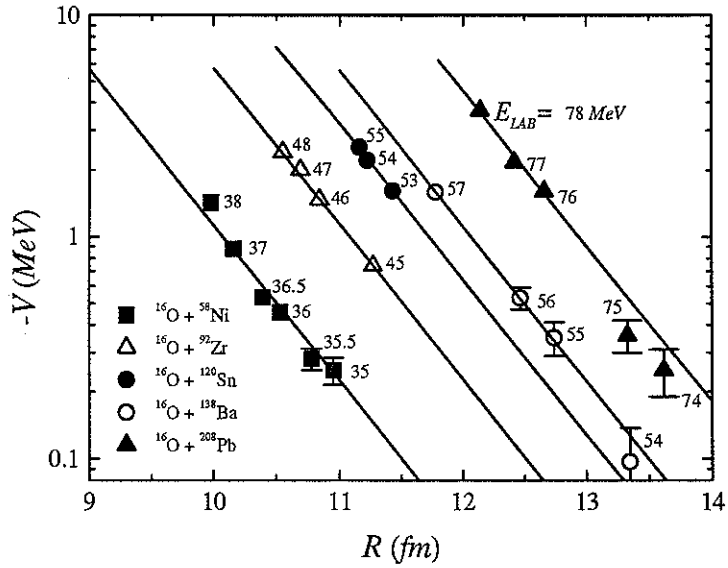


Figure 5: The nuclear potential strength as a function of the sensitivity radius for the $^{16}O + ^{58}Ni, ^{92}Zr, ^{120}Sn, ^{138}Ba$ and $^{208}Pb$ systems. The bombarding energies of the elastic scattering angular distributions in which the sensitivity radii have been obtained are indicated in the figure. The solid lines represent potentials with the same diffuseness value, $\overline{a} = 0.62\ fm$.

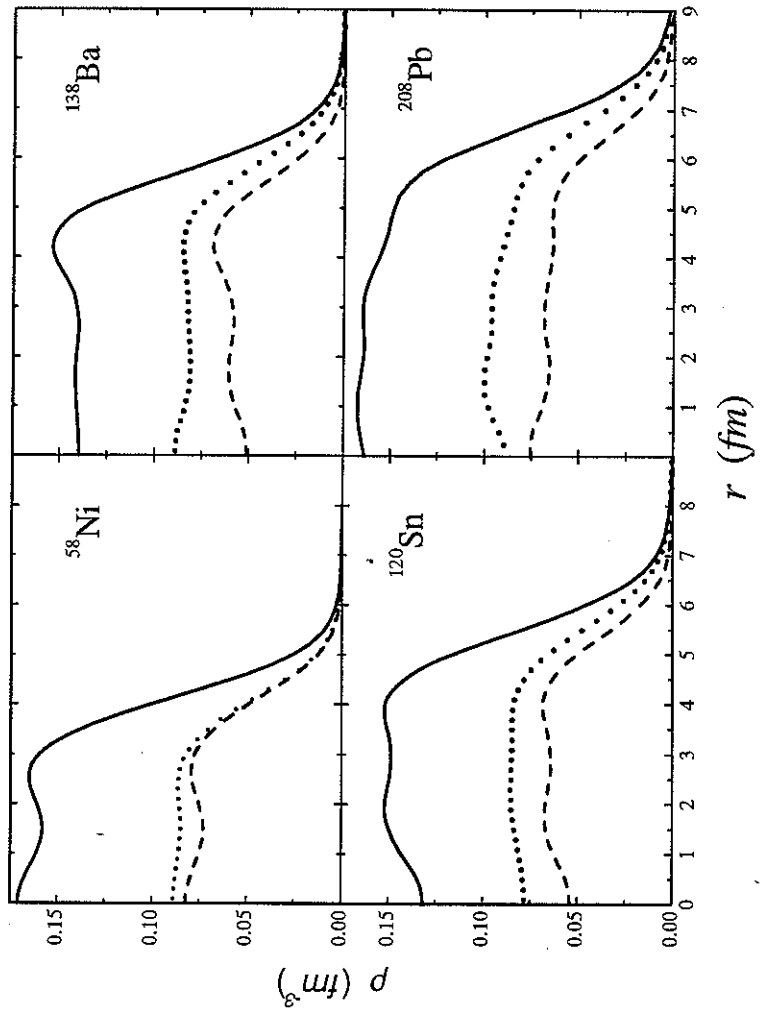


Figure 6: The ground-state proton (dashed lines), neutron (dotted lines) and total (solid lines) densities derived from theoretical calculations for the $^{58}$Ni, $^{120}$Sn, $^{138}$Ba and $^{208}$Pb nuclei. The $^{58}$Ni and $^{208}$Pb densities were obtained from Refs. [2] and [10], respectively. The densities for the neutron ($^{120}$Sn) and proton ($^{138}$Ba ) superfluid nuclei were calculated using a self-consistent Dirac-Hartree-Bogoliubov model [11].

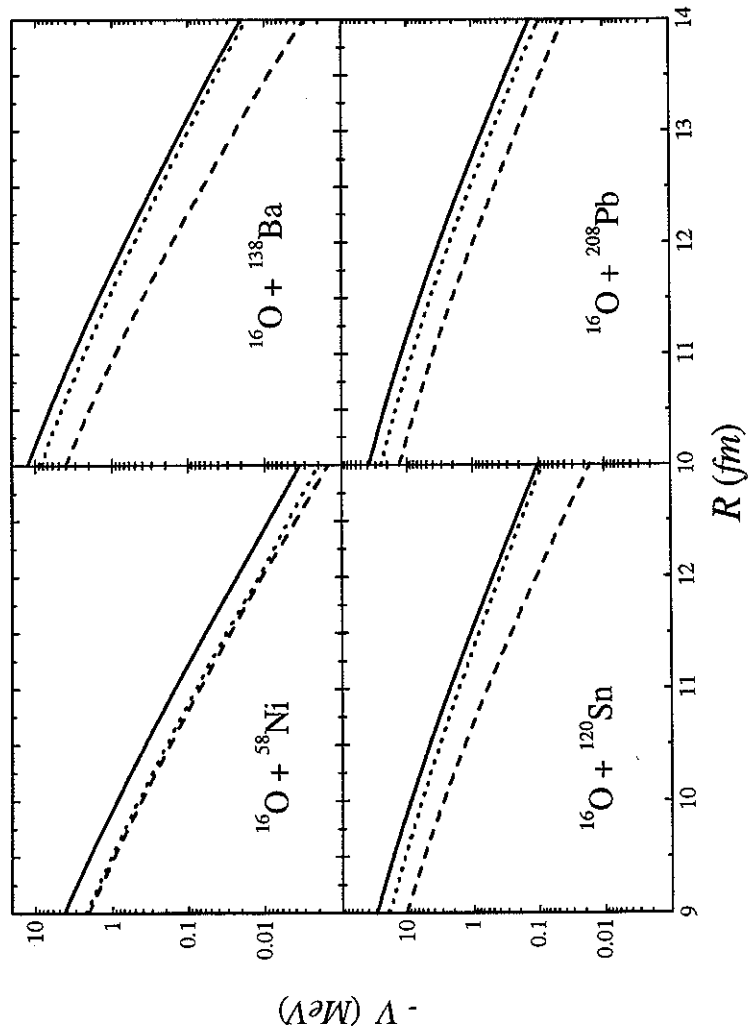


Figure 7: Proton (dashed lines), neutron (dotted lines) and total (solid lines) double-folding potentials at the surface region for the $^{16}O + ^{58}Ni, ^{120}Sn, ^{138}Ba$ and $^{208}Pb$ systems (see text for details).

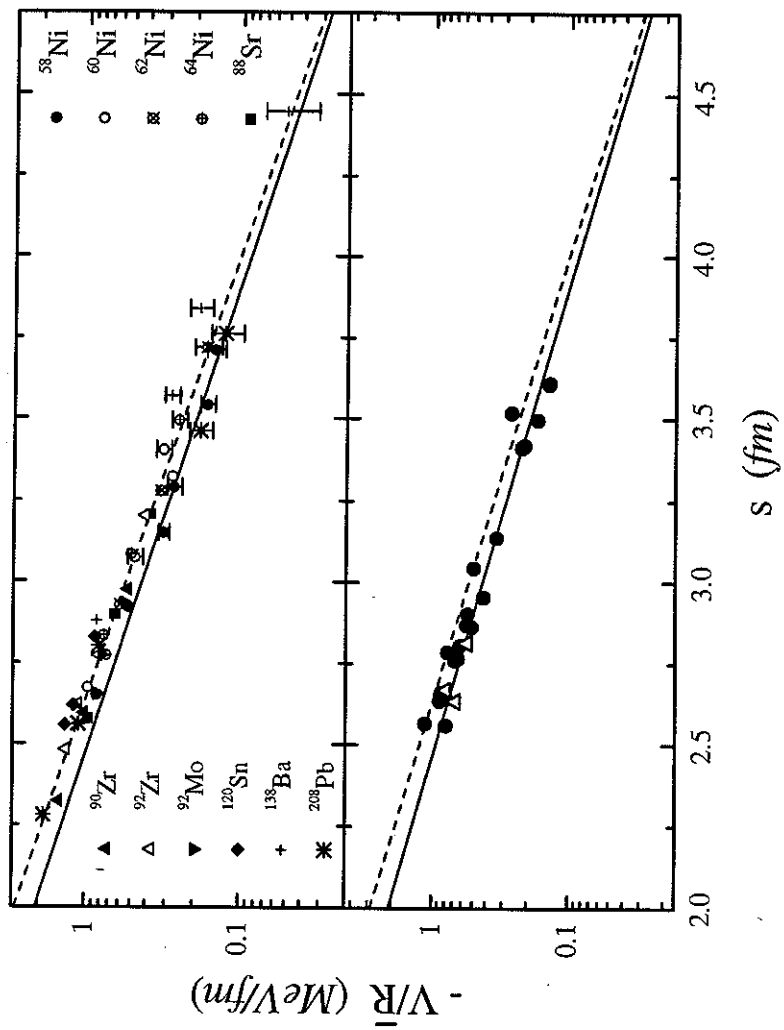


Figure 8: The "normalized" potential strengths ($V/\bar{R}$) from sub-barrier (top) and above-barrier (bottom) elastic scattering data analyses as a function of the nucleus surface separation distance ($s$) for systems that involve the $^{16}$O nucleus. The open triangles (bottom) represent potential strengths deduced from earlier [15, 16] OM analyses of the angular distributions presented in Fig. 9. The Christensen and Winther's (CW) empirical potential [5] is represented by solid lines. The dashed lines represent a fit of the sub-barrier potential strengths by Eq. (9).

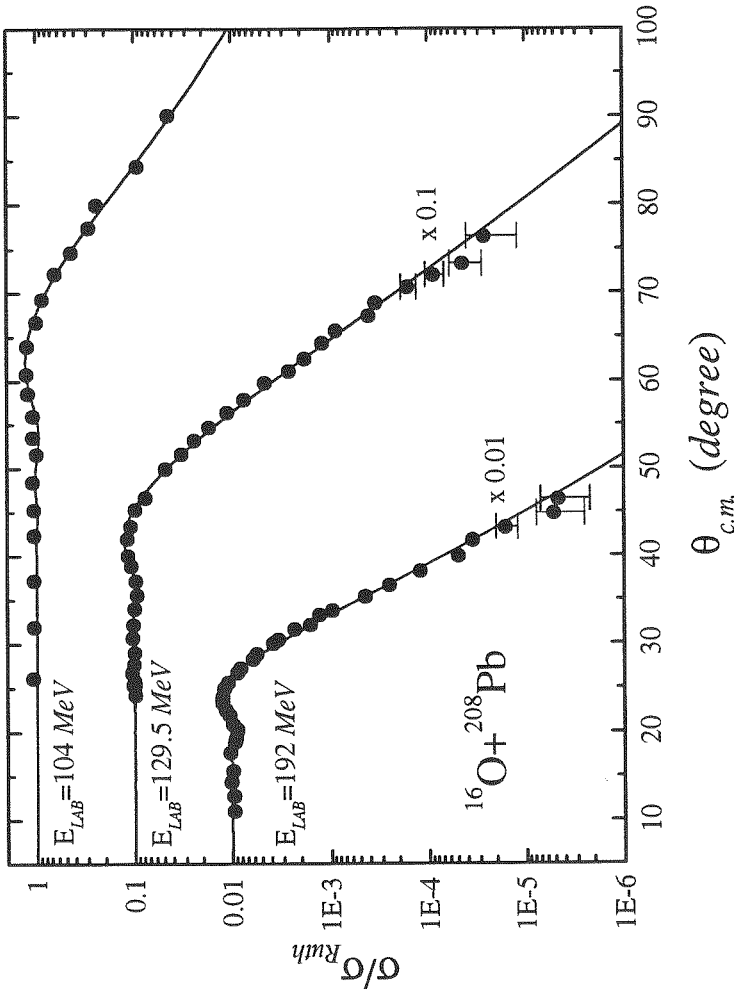


Figure 9: Elastic scattering angular distributions for the $^{16}O$ + $^{208}Pb$ system at the energies $E_{LAB}$ = 104, 129.5 and 192 $MeV$ (the data were extracted from Refs. [15, 16]). The solid lines represent data fits, in which the sub-barrier energy-independent nuclear potential was assumed for the real part of the optical potential. In the data fits, only the diffuseness and depth parameters of the Woods-Saxon shape imaginary potential were allowed to vary.

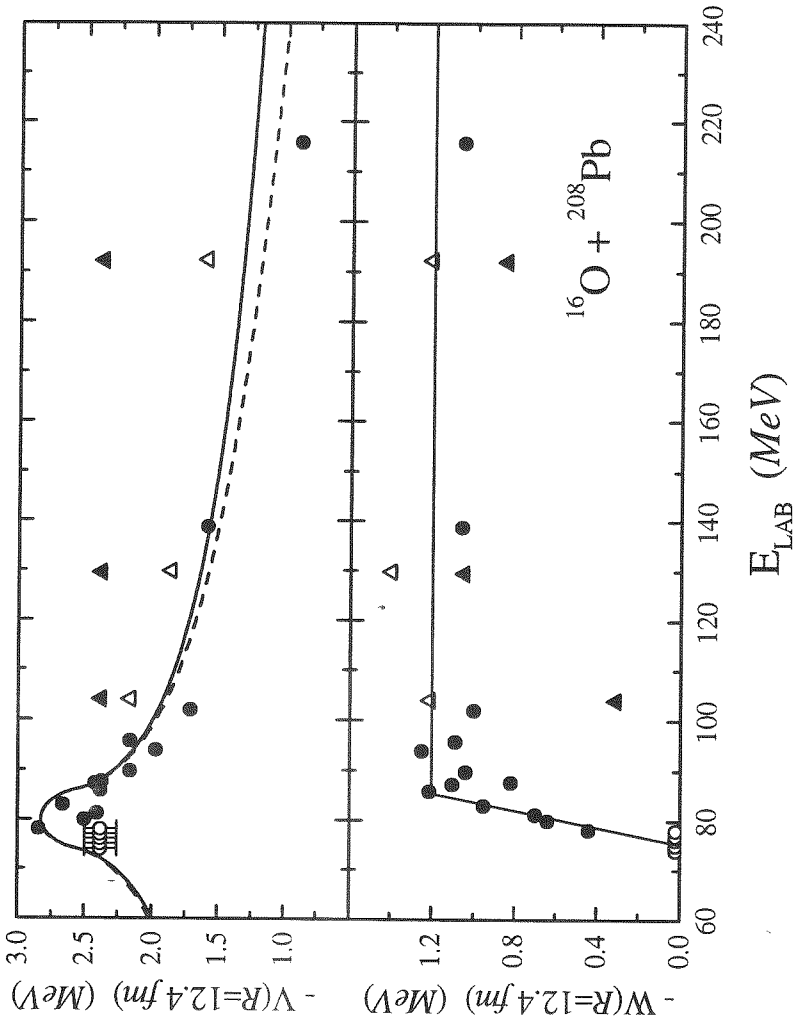


Figure 10: Potential strength values obtained from earlier [7] OM data analyses of elastic scattering angular distributions at energies above the barrier (closed circles and open triangles). The open circles represent the energy-independent nuclear potential that we have obtained from sub-barrier data analyses. The open triangles correspond to earlier [7] data analyses of the angular distributions presented in Fig. 9. The closed triangles correspond to present OM analyses of the same angular distributions (see text for details). The lines represent behaviors compatible with the dispersion relation, with (dashed line) and without (solid line) the additional effect due to the nonlocal nature of the bare potential.

**Table 1:** The diffuseness values of the nuclear potentials from Optical Model data analyses ($a$) and Double-Folding calculations ($a_f$), and the radii ($R_{1\ MeV}$) at which the strengths of the OM energy-independent nuclear potentials equal 1 $MeV$. In the calculations of the $R_{1\ MeV}$ values, $\overline{a} = 0.62\ fm$ was assumed to be the diffuseness for the OM nuclear potentials. The strengths of the folding ($V_f$) and proximity ($V_{pr}$) potentials at the radii $R_{1\ MeV}$ are also included in the table.

| target | $a\ (fm)$ | $a_f\ (fm)$ | $R_{1\ MeV}\ (fm)$ | $V_f\ (MeV)$ | $V_{pr}\ (MeV)$ |
|---|---|---|---|---|---|
| $^{58}$Ni | $0.57 \pm 0.03$ | 0.57 | 10.06 | 0.81 | 0.62 |
| $^{60}$Ni | $0.58 \pm 0.04$ | 0.58 | 10.21 | 0.72 | 0.55 |
| $^{62}$Ni | $0.60 \pm 0.05$ | 0.58 | 10.28 | 0.72 | 0.54 |
| $^{64}$Ni | $0.67 \pm 0.05$ | 0.59 | 10.39 | 0.67 | 0.50 |
| $^{88}$Sr | $0.71 \pm 0.05$ | 0.58 | 10.93 | 0.71 | 0.54 |
| $^{90}$Zr | $0.63 \pm 0.03$ | 0.59 | 10.98 | 0.70 | 0.55 |
| $^{92}$Zr | $0.61 \pm 0.05$ | 0.61 | 11.11 | 0.66 | 0.48 |
| $^{92}$Mo | $0.63 \pm 0.06$ | 0.59 | 10.99 | 0.73 | 0.57 |
| $^{120}$Sn | $0.59 \pm 0.07$ | 0.65 | 11.73 | 0.76 | 0.44 |
| $^{138}$Ba | $0.63 \pm 0.03$ | 0.61 | 12.07 | 0.60 | 0.42 |
| $^{208}$Pb | $0.56 \pm 0.04$ | 0.63 | 12.94 | 0.75 | 0.49 |

**Table 2:** The table presents the diffuseness ($a_i$) and depth ($W_0$) parameters of the imaginary part of the OM potential, obtained from the fit of elastic scattering angular distributions for the $^{16}$O + $^{208}$Pb system at $E_{LAB} = 104$, 129.5 and 192 $MeV$. In these fits, the energy-independent ($V_{SB}$) nuclear potential, obtained from the sub-barrier data analyses, was assumed for the real part of the optical potential. Also the strong absorption radii ($R_{SA}$), the corresponding potential strengths from the Christensen and Winther's systematization ($V_{CW}$), and the sub-barrier potential ($V_{SB}$) at $R_{SA}$ are included in the table.

| $E_{LAB}\ (MeV)$ | $a_i\ (fm)$ | $W_0\ (MeV)$ | $R_{SA}\ (fm)$ | $V_{CW}\ (MeV)$ | $V_{SB}\ (MeV)$ |
|---|---|---|---|---|---|
| 104.0 | 0.316 | 951 | 12.672 | 1.088 | 1.541 |
| 129.5 | 0.523 | 102 | 12.520 | 1.557 | 1.968 |
| 192.0 | 0.443 | 176 | 12.493 | 1.324 | 2.056 |